

## FLOW STRUCTURE CHARACTERISTICS OF TURBULENT BOUNDARY LAYER MODIFIED BY MINIATURE VORTEX GENERATORS

**C. I. Chan**

School of Mechanical Engineering  
University of Adelaide  
South Australia 5005, Australia  
chiip.chan@adelaide.edu.au

**R. C. Chin**

School of Mechanical Engineering  
University of Adelaide  
South Australia 5005, Australia  
rey.chin@adelaide.edu.au

### ABSTRACT

In this study we investigate the passive control of a turbulent boundary layer using miniature vortex generator (MVG), which consists of pairs of winglets or rectangular blades arranged in spanwise oriented arrays in the flow. A well-resolved large-eddy simulation of rectangular MVGs in a spatially evolving moderate Reynolds number zero pressure gradient turbulent boundary layer up to  $Re_\tau = 1350$  is performed. Preliminary results are presented on the different flow characteristics related to the large streamwise extent high and low-momentum regions (HSR and LSR) introduced by the MVG. We further employ a triple velocity decomposition to investigate the turbulent boundary layer modifications. The instantaneous velocity fluctuation is decomposed into a turbulent velocity component and a spatial component, where the latter represents a spatial variation of the time-averaged flow produced by the MVG. The turbulent velocity fluctuations associated with the HSR and LSR are further investigated using proper orthogonal decomposition (POD). The POD analysis aims to decompose the velocity fluctuation field in terms of a set of basis function, which contains the temporal and spatial information of the dominant structures in the flow. We further examine based on this, a reduced-order reconstruction of the HSR and LSR, using one-dimensional and two-dimensional data.

### INTRODUCTION

The miniature vortex generator (MVG) is a passive device capable of generating streamwise orientated vortices and give rise to long and persistent streamwise streaks that evolve downstream in boundary layer flows. The MVG remains a possible solution for effective flow control because of its simplicity and cost effectiveness. The effects of MVGs upon laminar boundary layers developed on flat plates have been well explored and understood both experimentally and numerically (Fransson & Talamelli, 2012; Shahinfar *et al.*, 2012). They are well known to delay flow transition from laminar to turbulent through stabilizing the growth of Tollmien–Schlichting (TS) waves and oblique disturbance, thereby resulting in a substantial skin friction re-

duction (Fransson *et al.*, 2006; Fransson & Talamelli, 2012; Shahinfar *et al.*, 2012, 2014; Sattarzadeh *et al.*, 2014). However, the same may not be true for flow that is fully turbulent.

Recent experimental studies (Lögberg, 2006; Lögberg *et al.*, 2009) on MVGs were conducted to investigate flow separation controls by vortex generators in adverse- and zero-pressure gradient turbulent boundary layers and it has been shown that the induced high and low-momentum regions persist for up to  $300h$  (where  $h$  is the device height). It would be worthwhile to pursue a study on the streamwise evolution and behaviour of the induced high and low-momentum regions in more detail. In addition, triple velocity decomposition should be considered when flow exhibits spatial heterogeneity perpendicular to the flow direction (e.g. spanwise periodicity) (Coceal & Belcher, 2004). The total velocity fluctuations can be decomposed into a turbulent and coherent fluctuations. The coherent fluctuation arise due to spanwise periodicity introduced by MVG can be treated in a similar fashion, as demonstrated by Shahinfar *et al.* (2013) and recently by Chan & Chin (2022). In the present study, the velocity fluctuation fields of the low-speed and high-momentum regions are first decomposed based on the triple decomposition. To further investigate their similarity and difference, the proper orthogonal decomposition is then employed.

### NUMERICAL PROCEDURE

In the following, the streamwise, wall-normal and spanwise coordinates are denoted as  $x$ ,  $y$  and  $z$ , and their velocity components are denoted by  $u$ ,  $v$  and  $w$ , respectively. Time-averaged velocity is denoted by a  $(\bar{\cdot})$  or a capital letter e.g.  $U = \bar{u}$ , and fluctuation is denoted by a prime ( $\cdot'$ ). The symbol  $\langle \cdot \rangle$  denotes a global mean value over the span.

A numerical simulation of miniature vortex generators (MVG) set up in a moderate Reynolds number zero-pressure-gradient turbulent boundary layer (TBL) was performed. This simulation was motivated by recent experimental studies of Lögberg *et al.* (2009), Sattarzadeh *et al.* (2014) and Sattarzadeh & Fransson (2015). The MVG configuration is

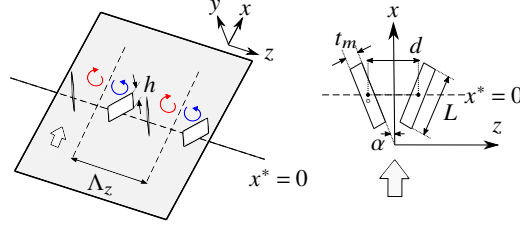


Figure 1: Schematic of the MVG layouts considered in the present study. The MVG parameters are scaled by the inlet displacement thickness  $\delta_0^*$ :  $h = 4$  is the blade height,  $t_m = 1$  is the blade width,  $L = 10$  is the blade length,  $\alpha = 15^\circ$  is the angle of attack of the MVG with respect to the flow direction,  $d = 10$  is the spanwise distance between the centroids of blades in one pair and  $\Lambda_z = 40$  is the spanwise spacing between MVG pairs.

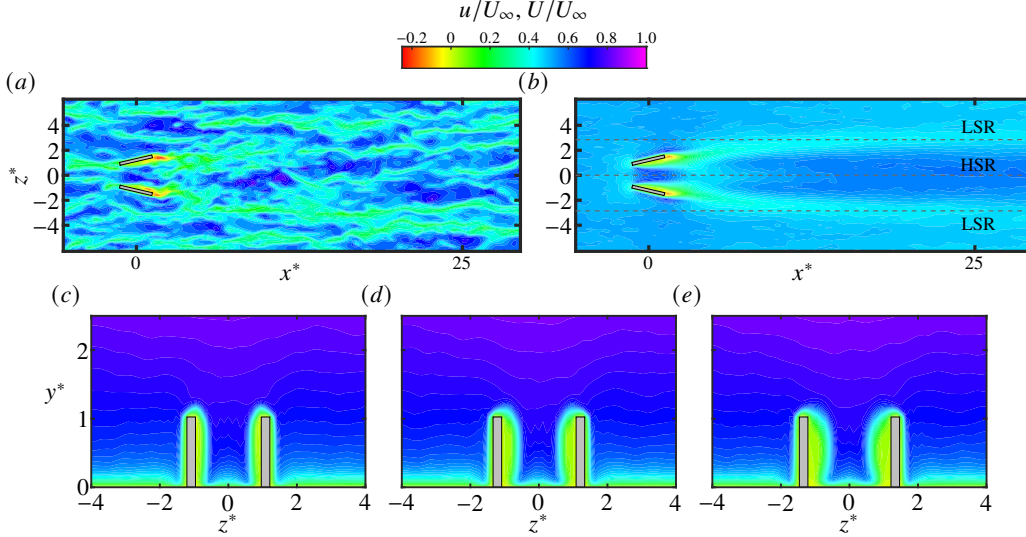


Figure 2: (a) Instantaneous realisation of the streamwise velocity flow field,  $u/U_\infty$ , at  $y^* = 0.25$  past a pair of MVG. Top view (b) and cross-section views of the time-averaged streamwise velocity flow field,  $U/U_\infty$ , at (c)  $x^* = -0.5$ , (d)  $x^* = 0$  and (e)  $x^* = 0.5$ , where  $x^* = (x - x_M)/h$  and  $z^* = z/h$ . Rectangular box outlines the MVG cross section. In (b), the dashed black lines mark the spanwise locations of high-speed region (HSR) and low-speed region (LSR), with secondary flows of common flow down and common flow up at  $x^* = 25$ , respectively.

shown in figure 1. The MVG array is positioned at  $x_M = 950\delta_0^*$  from the inlet (corresponds to  $Re_\tau = \delta^+ \approx 430$ , where  $\delta_0^*$  is the inlet displacement thickness and  $\delta$  is the boundary layer thickness). The MVG parameters that scaled by the inlet displacement thickness are respectively:  $h = 4$  is the blade height,  $t_m = 1$  is the blade thickness,  $L = 10$  is the blade length,  $\alpha = 15^\circ$  is the angle of attack of the MVG with respect to the flow direction,  $d = 10$  is the spanwise distance between the centroids of blades in one pair and  $\Lambda_z = 40$  is the spanwise spacing between MVG pairs. Large-eddy simulation of the turbulent boundary layer was performed using a fully spectral numerical code (Chevalier *et al.*, 2007). A sub-grid-scale approximate deconvolution model (ADM-RT) has been employed to compute approximations to the unfiltered solutions of the incompressible continuity and Navier-Stokes equations by a repeated filter operation, i.e.

$$\frac{\partial \hat{u}_i}{\partial x_i} = 0, \quad (1)$$

$$\frac{\partial \hat{u}_i}{\partial t} + \hat{u}_j \frac{\partial \hat{u}_i}{\partial x_j} + \frac{\partial \hat{p}}{\partial x_i} - \frac{1}{Re} \frac{\partial^2 \hat{u}_i}{\partial x_j \partial x_j} = -\chi H_N \otimes \hat{u}_i, \quad (2)$$

with superscripts  $\wedge$  refer to a resolved-scale, and  $\otimes$  denotes

the convolution and the relaxation term  $-\chi H_N \otimes \hat{u}_i$ :  $\chi$  is the model coefficient; and  $H_N \otimes \hat{u}_i$  is the high-pass approximately deconvolved quantities. The ADM-RT model has been widely used for performing incompressible transitional and turbulent flows simulations (Stolz *et al.*, 2001; Schlatter *et al.*, 2004; Eitel-Amor *et al.*, 2014; Schlatter *et al.*, 2010). Spatial discretisation is based on a Fourier series with 3/2 zero-padding for de-aliasing in the streamwise ( $x$ ) and spanwise ( $z$ ) directions, and a Chebyshev polynomial is employed in the wall-normal direction ( $y$ ). The computational domain in the streamwise, wall-normal and spanwise directions are respectively:  $x_L \times y_L \times z_L = 6000\delta_0^* \times 200\delta_0^* \times 360\delta_0^*$  using  $6144 \times 513 \times 768$  spectral modes. This give uniform grid spacings of  $\Delta x^+ \approx 16.9$  and  $\Delta z^+ \approx 8.1$  in the streamwise and spanwise directions (the superscript  $+$  refers to scaling with the friction velocity  $u_\tau = \sqrt{\tau_w/\rho}$  and kinematic viscosity  $\nu$ , where  $\tau_w$  is the wall shear stress and  $\rho$  is the fluid density). In the wall-normal direction, there is a minimum of 15 Chebyshev collocation points within the region  $y^+ < 10$ . The first grid point away from the wall is at  $y^+ \approx 0.03$ , and the maximum spacing is  $\Delta y_{\max}^+ = 10.6$ . The time advancement is carried out by a second-order Crank-Nicolson scheme for the viscous terms and a third-order four-stage Runge-Kutta scheme for the non-linear terms (Chevalier *et al.*, 2007). Details on the numerical procedure for the MVG can be found in Chan & Chin (2022).

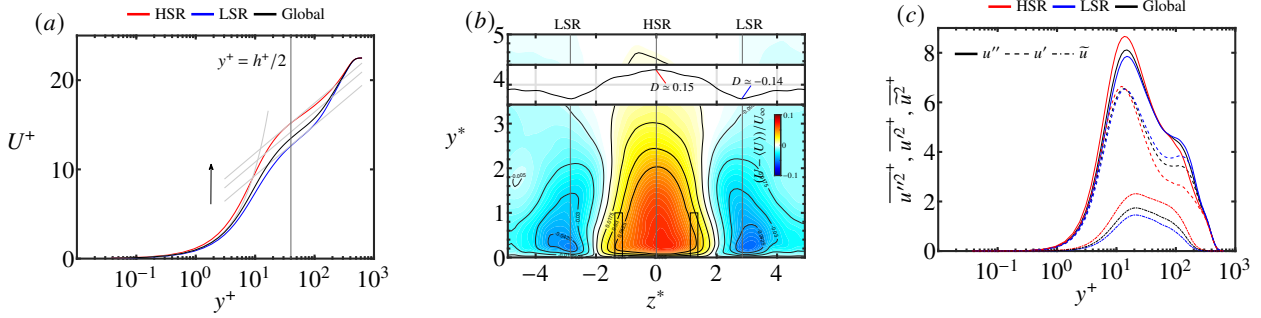


Figure 3: (a) Comparison of the time-averaged streamwise velocity at  $x^* = 25$ . The thick grey lines denote the linear and log-law regions  $1/\kappa \log y^+ + C$  with  $\kappa = 0.41$  and  $C = 3.7, 5.2$  and  $6.2$  in the arrow direction. (b) The velocity excess  $(U - \langle U \rangle)/U_\infty > 0$  associated with the high-speed region and the velocity deficit  $(U - \langle U \rangle)/U_\infty < 0$  associated with the low-speed region at  $x^* = 25$ . Inset shows the local spanwise skin friction variation at  $x^* = 25$ . (c) Comparison of the time-averaged streamwise velocity fluctuations:  $u''^2$ ,  $u'^2$  and  $\bar{u}^2$ .

Figure 2 shows instantaneous and time-averaged streamwise velocity fields obtained in the streamwise–spanwise plane at  $y/h = y^* = 0.25$  (figures 2a and 2b), and spanwise-wall-normal plane at  $x^* = -0.5, 0$  and  $0.5$  of the time-averaged streamwise velocity field (figures 2c, d, e), where  $x^* = (x - x_M)/h$  is defined at the centre of a MVG. Spanwise alternating high and low-speed patterns are observed with a high-speed region (denoted as HSR) formed along the centreline of the MVG, accompanied with low-speed region (LSR) to the side-by-side region.

## RESULTS AND DISCUSSIONS

### LSR and HSR

We present preliminary results of the mean and turbulent flow statistics of the HSR and LSR, respectively. Figure 3(a) shows differences of the time-averaged streamwise velocity between the HSR and LSR. The velocity defect in the mean flow profile can be estimated by comparing the downward shift of the log-law constants, as shown by the grey lines in figure 3(a). Vertical solid line denotes the wall-normal location  $y^* \approx 0.5$ , which yields  $\Delta \langle U \rangle^+ = -1.5$  at the LSR and  $\Delta \langle U \rangle^+ = 1.0$  at the HSR, respectively. The velocity defect is known to be related to the skin friction variation, where locally the skin friction is modified over the high- and low-speed regions along the spanwise direction. Low-speed fluid is lifted from the wall and reduces the streamwise wall shear stress  $\tau_w$  and results in substantial skin friction drag reduction. On the other hand, downwash motion transports the high-speed fluid towards the wall and increases the skin friction drag at the centre of an MVG pair. Figure 3(b) shows the velocity perturbation defined as  $(U - \langle U \rangle)/U_\infty$ , indicating the locations of the HSR and LSR and showing the presence of streamwise roll-modes induced downstream of the MVG. The inset in figure 3(b) shows the local spanwise skin friction variation at  $x^* = 25$ , defined as  $D(x, z^*) = (\bar{\tau}_w - \bar{\tau}_{w,0})/\bar{\tau}_{w,0}$ , where  $\bar{\tau}_w = \nu (d\bar{u}/dy)|_{y=0}$  is the time-averaged wall shear stress and  $z^* = z/h$ . The subscript 0 refers to the smooth case. The  $D > 0$  denotes the local increase and  $D < 0$  denotes the local drag reduction. We observe that HSR is associated with an increase of skin friction up to  $D \approx 0.15$  at  $z^* = 0$ , accompanied with a similar skin friction reduction rate centred at the LSR ( $z^* \approx \pm 3$ ). Finally, to further elucidate the physical modification of the MVG on the turbulent statistics we employed a similar approach to analyse roughness surface flow by triple decomposition of the velocity

components, which reads as:

$$\begin{aligned} u_i(x, y, z, t) &= \langle U_i \rangle(x, y) + u'_i(x, y, z, t) + \tilde{u}_i(x, y, z) \\ &= U_i(x, y, z) + u'_i(x, y, z, t), \end{aligned} \quad (3)$$

where the  $u'_i$  and  $\tilde{u}_i$  on the right-hand side of equation (3) are the turbulent fluctuation and MVG-induced fluctuation, respectively. The MVG-induced fluctuation  $\tilde{u}_i = U_i - \langle U_i \rangle$  is the spatial variation of the time-averaged flow due to MVG. The total fluctuation,  $u'_i = u'_i + \tilde{u}_i$  is equal to the turbulent fluctuation ( $u'_i$ ) for the smooth wall case since  $\tilde{u}_i = 0$ . The streamwise total stress  $\overline{u''u''}$ , Reynolds stress  $\overline{u'u'}$  and the MVG-induced stress  $\overline{\tilde{u}\tilde{u}}$  are presented in figure 3(c) for the HSR, LSR and the global (overall). Comparison of the MVG-induced stresses (red and blue dotted-dash lines) over the HSR and LSR suggests that the flow modification introduced by the MVGs on the HSR is quite different from that in the LSR, which also reflect on the differences between the turbulent stresses (red and blue dash lines). Further assessments are necessary to characterised their different flow behaviours.

### POD ANALYSIS OF LSR AND HSR

The proper orthogonal decomposition (POD) is used to investigate the differences in the flow characteristics associated with LSR and HSR. In the present study the data obtained from our numerical simulation the number of spatial points is larger than the number of snapshots. Therefore, the snapshot POD approach has been used and is briefly described here. Practically, the turbulent fluctuation was approximated by a finite sum of  $N$  expansion coefficients  $a_i$  and spatial modes  $\phi_i$  as:

$$u'(\mathbf{x}, t) \approx \sum_{i=1}^N a_i(t) \phi_i(\mathbf{x}). \quad (4)$$

The spatial modes  $\phi_i(\mathbf{x})$  were obtained from solving an eigenvalue problem of the correlation matrix of  $u'$ . The correlation matrix was calculated between individual snapshots of streamwise velocity fluctuation  $(u'(\mathbf{x}, t_1) = u'(\mathbf{x}, t_1), u'(\mathbf{x}, t_2), \dots)$  based on their temporal correlations. The correlation (temporal) matrix is given by:

$$\mathbf{M} = M_{ij} = \frac{1}{N_i - 1} [u'(\mathbf{x}, t_i), u'(\mathbf{x}, t_j)], \quad (5)$$

where  $N_t$  denotes the total number of snapshots and  $[\cdot]$  defines a dot product in the present study. The eigenvalue problem to be solved can be written as:

$$\mathbf{M}\boldsymbol{\psi}_i = \lambda_i\boldsymbol{\psi}_i. \quad (6)$$

The eigenvalues might be sorted in a descending order to relate to the energy content of the corresponding modes. Because we solve the eigenvalue problem based on temporal correlations, we need to project all the eigenmodes  $\boldsymbol{\psi}_i$  to the velocity field  $u'(\mathbf{x}, t_i)$  so that we can recover the first  $N_t$  spatial POD modes as

$$\boldsymbol{\phi}_j(\mathbf{x}) = \frac{\sum_i \boldsymbol{\psi}_j(t_i) u'(\mathbf{x}, t_i)}{\sqrt{\lambda_j} \sqrt{N_t - 1}}, \quad (7)$$

where the spatial POD modes are essentially orthonormal, i.e.  $[\boldsymbol{\phi}_i, \boldsymbol{\phi}_j] = \delta_{ij}$ . Finally, the expansion coefficients  $a_i$  can be obtained by projection of the velocity field on the spatial modes. In what follows, we will consider two cases. First, POD analysis results will be presented in figure 4 for a one-dimensional POD basis case, i.e.

$$u'(y, t) \approx \sum_{i=1}^N a_i(t) \phi_i(y), \quad (8)$$

where we treat  $u'(y, z^* = 0, t)$  and  $u'(y, z^* = -3, t)$  as two independent time series data representing the HSR and LSR, respectively. We tend to compare the similarities and differences of the POD modes in the wall-normal direction between HSR and LSR. Next, we will proceed to the two-dimensional case, i.e.

$$u'(y, z, t) \approx \sum_{i=1}^N a_i(t) \phi_i(y, z), \quad (9)$$

where we further examined the correlation to include the spanwise direction  $u'(y, |z^*| \leq 5, t)$ .

### 1D POD

The first six one-dimensional POD modes of the HSR and LSR are shown in figure 4(a). Results show that the difference in the decompositions between HSR and LSR is quite small, which might be expected because both HSR and LSR arise from a pair of symmetrical streamwise vortices generated by the MVG. Figure 4(b) shows percentage contribution of the eigenvalues of the first 100 one-dimensional POD modes of the HSR and LSR. The first 100 modes of the HSR and LSR contain roughly 35% of the total energy, mainly reside at the near-wall region  $y^+ \approx 15$ , as shown in figure 4(a). Figure 4(a, b) suggest that it is difficult to distinguish between HSR and LSR velocity fluctuations using only one-dimensional POD. Figure 4(c) shows a simple low-order reconstructions of the turbulent fluctuation in the HSR and LSR, using a reduced number of POD modes (e.g. Weiss *et al.*, 2022), i.e.,

$$u' \sim u'_{N_R}(\mathbf{x}, t) = \sum_{i=1}^{N_R} a_i(t) \boldsymbol{\phi}_i(\mathbf{x}), \quad (10)$$

where  $N_R = 1, 2, \dots$ , denotes the number of modes for reconstruction. Alternately, it is common to reconstruct a low-order model using the Galerkin projection in the literature, where the Navier–Stokes equations are first expressed in terms of POD basis, and by taking an inner product of resulting equations with the POD modes, a system of ordinary differential equations for the  $a_i(t)$  is obtained (e.g. Rowley *et al.*, 2004). Results show that the first 10 modes reconstruction is a fairly good approximation of the intensity profile, where they contribute to almost 95% of the total energy (as shown in figure 4(b)), i.e.,

$$\frac{[u'_{N_R}(\mathbf{x}, t_i), u'_{N_R}(\mathbf{x}, t_i)]}{[u'(\mathbf{x}, t_i), u'(\mathbf{x}, t_i)]} = \sum_i^{N_R} \lambda_i / \sum_i^N \lambda_i, \quad (11)$$

and  $\overline{a_i(t)a_j(t)} = \lambda_i \delta_{ij}$ . Figure 4(c) also demonstrates how the reconstructed intensity profile vary with increasing number of modes, particularly at the near-wall peak  $y^+ \approx 15$  and outer region  $y/\delta \approx 0.2$  ( $y^+ \approx 120$ ), where the latter is clearly associated with the first two POD modes. Interestingly, the intensity of the inner peak seems to shift towards  $y^+ \approx 15$  when higher modes are used in the reconstruction (marked as  $\diamond$  in figure 4c).

### 2D POD

Next we consider POD in spanwise and wall-normal directions (9). It is not surprised to observe that the differences between the flow characteristics in the HSR and LSR become much clearer. The first six POD modes  $\phi_i(y, z)$  are presented in figure 5 ranked according to the eigenvalues. The first POD mode appear to be anti-correlated in between HSR and LSR, associating with a symmetrical streamwise vortices pair originating from the MVG. A visual inspection of the spanwise separation between the same sign of correlation regions implies that  $\lambda_z \approx \Lambda_z/2$ , reflecting the spanwise wavelength of the energy peak at the dominant spanwise mode observed in (Chan & Chin, 2022), even though the first POD mode itself contributes to only 6% of the total energy. The percentage contribution of the first 100 POD modes is plotted in figure 4(b) in a comparison with the 1D case. It can be seen that the contribution of the first six modes to the total energy is approximately 25% and up to 80% for the first 100 modes. Figure 6 shows the velocity reconstruction of the HSR ( $z^* = 0$ ) and LSR ( $z^* \approx -3$ ) obtained using 2D POD modes. The blue line in figure 6(a) suggests that  $u'_{N_R=1} \approx 0$ . This is attributed to  $\phi_1(y, z^* = 0) \approx 0$  as shown in figure 5 (illustrated as vertical dashed line). On the other hand, the vertical solid line represents the reconstruction of the LSR based on  $\phi_1(y, z^* = -3)$ , plotted as intensity profile in figure 6(b) (blue line).

### CONCLUSIONS

In this study we focused on the flow behaviour of the long streamwise extended and spanwise periodic high and low-momentum regions produced by the MVGs. A large-eddy simulation of rectangular MVGs positioned in a spatially evolving moderate Reynolds number zero pressure gradient turbulent boundary layer up to  $Re_\tau = 1350$  was performed (Chan & Chin, 2022). The fluctuating velocity field associated with the HSR and LSR are first extracted by a triple velocity decomposition, then we analysed their velocity fluctuations using proper orthogonal decomposition in the (i) wall-normal direction and (ii) spanwise and wall-normal directions. A comparison of the POD modes between the 1D and 2D cases shows that in the 1D case the modes  $\phi_i(y)$  and eigenvalue ratio associated with the HSR and LSR are similar. This is because

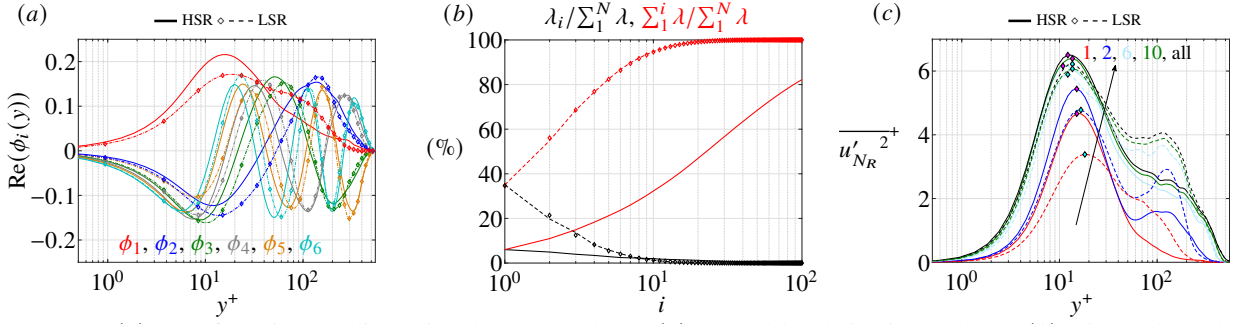


Figure 4: (a) The first six one-dimensional POD modes  $\phi_i(y)$  ranked by their eigenvalues. (b) Eigenvalues (black) and cumulative sum of the eigenvalues (red) in 1D case for HSR (---) and LSR ( $\diamond$ ), respectively. The eigenvalues (black) and cumulative sum of the eigenvalues (red) for two-dimensional POD modes are shown in (—). (c) Low-order reconstruction of turbulent intensity using the first  $N_R$  one-dimensional POD modes:  $N_R = 1, 2, 6, 10$  and all (in the arrow direction).

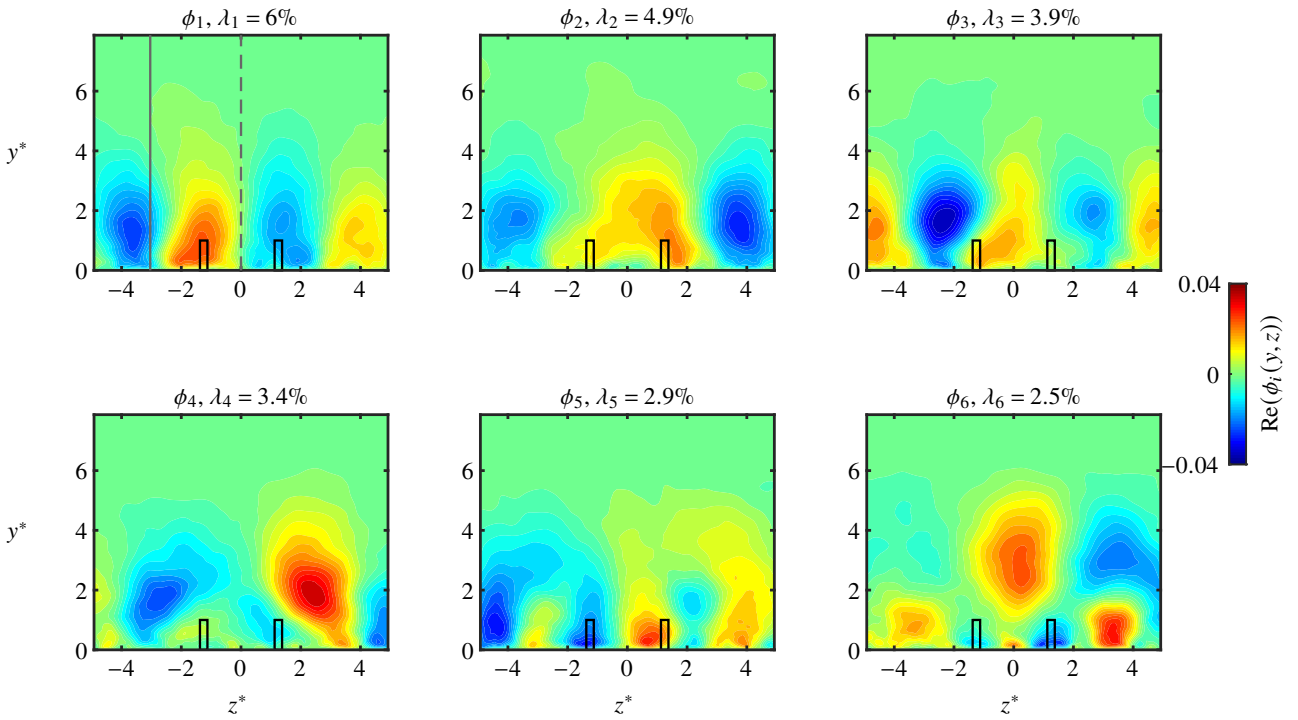


Figure 5: The first six two-dimensional POD modes  $\phi_i(y, z)$  with their eigenvalues ranked by percentage contributions.

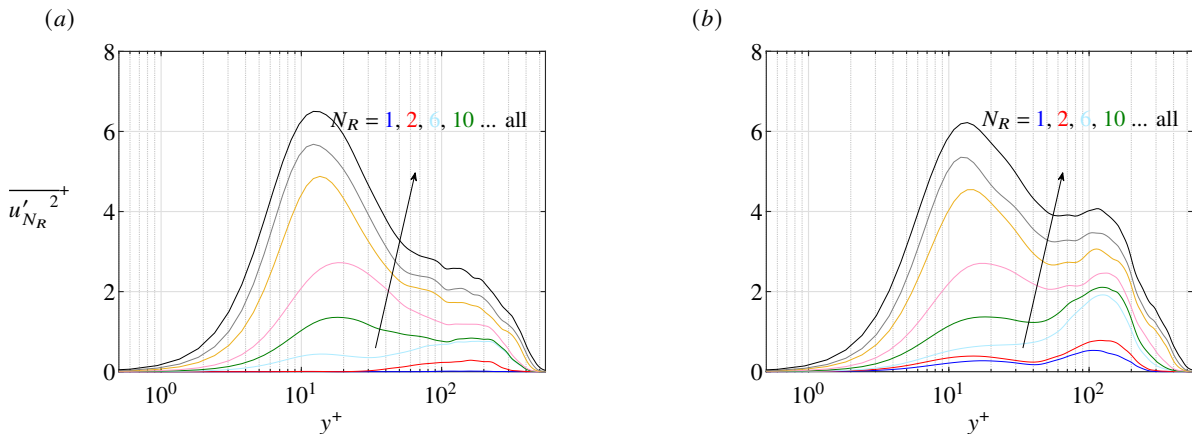


Figure 6: Low-order reconstruction of turbulent intensity using the first  $N_R$  two-dimensional POD modes:  $N_R = 1, 2, 6, 10, 20, 50, 100$  and all (in the arrow direction). (a) HSR and (b) LSR.

spanwise correlation was not considered in the 1D case. The major difference between the HSR and LSR is that when taking into account of the expansion coefficient, the low-order velocity

reconstruction are found to be quite different, as shown in figure 4(c). Example of time traces of expansion coefficient  $a_1(t)$  is plotted in figure 7. On the other hand, for the 2D case, the first

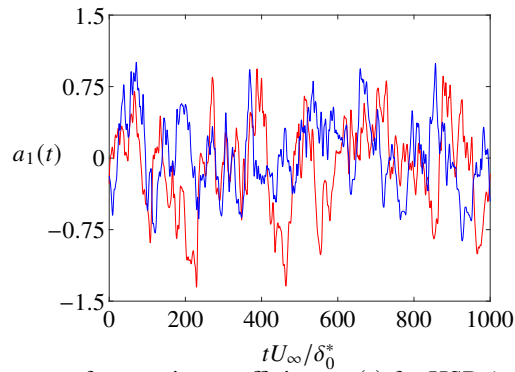


Figure 7: Time traces of expansion coefficient  $a_1(t)$  for HSR (red) and LSR (blue).

few modes show similarly that alternating spatial patterns with opposite sign spaced in the spanwise direction, where the HSR and LSR are localised at the interface between these regions and indicate that the velocity fluctuations are anti-correlated.

## ACKNOWLEDGEMENTS

This research was undertaken with the assistance of resources provided at the NCI NF through the Computational Merit Allocation Scheme, supported by the Australian Government and the Pawsey Supercomputing Centre. Funds provided by the Australian Research Council are gratefully acknowledged.

## REFERENCES

- Chan, C. I. & Chin, R. C. 2022 Investigation of the influence of miniature vortex generators on the large-scale motions of a turbulent boundary layer. *J. Fluid Mech.* **932**, A29.
- Chevalier, M., Lundbladh, A. & Henningson, D. S. 2007 Simson—a pseudo-spectral solver for incompressible boundary layer flow. Tech. Rep. TRITA-MEK 2007:07. KTH Mechanics, Stockholm, Sweden.
- Coccal, O. & Belcher, S. E. 2004 A canopy model of mean winds through urban areas. *Q. J. R. Meteorol. Soc.* **130** (599), 1349–1372.
- Eitel-Amor, G., Örlü, R. & Schlatter, P. 2014 Simulation and validation of a spatially evolving turbulent boundary layer up to  $Re_\theta = 8300$ . *Intl J. Heat Fluid Flow* **47**, 57–69.
- Fransson, J. H. M. & Talamelli, A. 2012 On the generation of steady streamwise streaks in flat-plate boundary layers. *J. Fluid Mech.* **698**, 211–234.
- Fransson, J. H. M., Talamelli, A., Brandt, L. & Cossu, C. 2006 Delaying transition to turbulence by a passive mechanism. *Phys. Rev. Lett.* **96**, 064501.
- Lögberg, O. 2006 Vortex generators and turbulent boundary layer separation control. Licentiate thesis, Department of Mechanics, KTH, Stockholm.
- Lögberg, O., Fransson, J. H. M. & Alfredsson, P. H. 2009 Streamwise evolution of longitudinal vortices in a turbulent boundary layer. *J. Fluid Mech.* **623**, 27–58.
- Rowley, Clarence W., Colonius, Tim & Murray, Richard M. 2004 Model reduction for compressible flows using pod and galerkin projection. *Physica D: Nonlinear Phenomena* **189** (1), 115–129.
- Sattarzadeh, S. S. & Fransson, J. H. M. 2015 On the scaling of streamwise streaks and their efficiency to attenuate Tollmien–Schlichting waves. *Exp. Fluids* **56** (3), 1–16.
- Sattarzadeh, S. S., Fransson, J. H. M., Talamelli, A. & Fallenius, B. E. G. 2014 Consecutive turbulence transition delay with reinforced passive control. *Phys. Rev. E* **89**, 061001.
- Schlatter, P., Li, Q., Brethouwer, G., Johansson, A. V. & Henningson, D. S. 2010 Simulations of spatially evolving turbulent boundary layers up to  $Re_\theta = 4300$ . *Intl J. Heat Fluid Flow* **31** (3), 251–261.
- Schlatter, P., Stolz, S. & Kleiser, L. 2004 LES of transitional flows using the approximate deconvolution model. *Intl J. Heat Fluid Flow* **25** (3), 549–558.
- Shahinfar, S., Fransson, J. H. M., Sattarzadeh, S. S. & Talamelli, A. 2013 Scaling of streamwise boundary layer streaks and their ability to reduce skin-friction drag. *J. Fluid Mech.* **733**, 1–32.
- Shahinfar, S., Sattarzadeh, S. S. & Fransson, J. H. M. 2014 Passive boundary layer control of oblique disturbances by finite-amplitude streaks. *J. Fluid Mech.* **749**, 1–36.
- Shahinfar, S., Sattarzadeh, S. S., Fransson, J. H. M. & Talamelli, A. 2012 Revival of classical vortex generators now for transition delay. *Phys. Rev. Lett.* **109**, 074501.
- Stolz, S., Adams, N. A. & Kleiser, L. 2001 An approximate deconvolution model for large-eddy simulation with application to incompressible wall-bounded flows. *Phys. Fluids* **13** (4), 997–1015.
- Weiss, Julien, Steinfurth, Ben, Chamard, Léo, Giani, Alain & Combette, Philippe 2022 Spectral proper orthogonal decomposition of unsteady wall shear stress under a turbulent separation bubble. *AIAA Journal* **60** (4), 2150–2159.